Faraday Acceleration with Radio-Frequency Assisted Discharge

Edgar Y. Choueiri* and Kurt A. Polzin†
Princeton University, Princeton, New Jersey 08544

A new electrodeless accelerator concept that relies on an rf-assisted discharge, an applied magnetic field, and electromagnetic acceleration using an inductive coil is presented. The presence of a preionized plasma allows for current sheet formation at lower discharge voltages and energies than those found in other pulsed inductive accelerator concepts. A proof-of-concept experiment, supported by optical and probe diagnostics, has been constructed and used to demonstrate low-voltage, low-energy current sheet formation and acceleration. Magnetic field data indicate that the peak sheet velocity in this unoptimized configuration operating at a pulse energy of 78.5 J is 12 km/s. Visual observations indicate that plasma follows the applied magnetic field from the rf discharge to the face of the planar acceleration coil, while magnetic field probing and visualization using a fast-framing camera show the formation and acceleration of the current sheet.

Nomenclature

B	=	magnetic field, G
C	=	capacitance, F
I, J	=	current, A
j	=	current density, A m^{-2}
L_c	=	coil inductance, H
L_0	=	external inductance, H
M	=	mutual inductance, H
R_e	=	external resistance, Ω
R_p	=	plasma resistance, Ω
r	=	radial coordinate, m
V_0	=	initial voltage, V
z	=	axial coordinate, m
z_{emc}	=	electromagnetic coupling length scale, m
ΔL	=	change in circuit inductance, H
Δt_a	=	acceleration coil pulse length, s
Δt_g	=	gas pulse length, s
Δt_{RF}	=	rf pulse length, s
μ	=	magnetic permeability, H m^{-1}
ρ_0	=	gas density, kg m^{-3}

Subscripts

Applied	=	applied magnetic field component
Coil	=	acceleration coil component
r	=	radial component
z	=	axial component
θ	=	azimuthal component

I. Introduction

PULSED inductive plasma accelerators are spacecraft propulsion devices in which energy is stored in a capacitor and then discharged through an inductive coil. The device is electrodeless, inducing a current in a plasma located near the face of the coil. The propellant is accelerated and expelled at a high exhaust velocity [$\mathcal{O}$ (10 km/s)] through the interaction of the plasma current and the induced magnetic field.

Inductive plasma accelerators are attractive as propulsive devices for many reasons. The lifetime and contamination issues associated with electrode erosion in conventional pulsed plasma thrusters (PPTs) do not exist in devices where the discharge is inductively driven. In addition, a wider variety of propellants (e.g., CO_2, H_2O) becomes available for use when compatibility with metallic electrodes is no longer an issue. Moreover, pulsed inductive accelerators (indeed, pulsed accelerators in general) can maintain the same performance level over a wide range of input power levels by adjusting the pulse rate.

We introduce a new pulsed inductive plasma accelerator concept, the Faraday accelerator with radio-frequency assisted discharge (FARAD).[1] In this work we describe the results from a proof-of-concept experiment and not a working, optimized thruster. In the rest of this section, we describe the FARAD concept and provide motivation for our research.

A. Description of the Concept

A schematic representation of the FARAD proof-of-concept experiment is shown in Fig. 1. In the schematic two joined cylindrical glass tubes form a vacuum chamber for the experiment. Plasma generation occurs in the smaller vessel while acceleration takes place in the larger-diameter, adjoining vessel. The chamber is surrounded by a set of applied B-field electromagnet coils, which are configured to produce a highly axial field inside the smaller tube and a highly diverging, mostly radial field near the flat backend of the larger vessel, as shown by the representative applied B-field lines drawn in the figure.

In a FARAD thruster, gas is injected into the smaller tube (from the left in the picture) and is ionized by a helicon discharge, which requires the applied axial magnetic field and an rf/helicon antenna; the latter is shown wrapped around the outside of the smaller tube. A helicon discharge[2–4] is a radio-frequency inductive discharge that is very efficient as a plasma source. The highly ionized plasma is guided by the applied magnetic field to flow radially outward along the flat backend of the adjoining larger vessel.

A flat inductive coil is mounted on the outer side of the backend (which protects the coil from the plasma). The coil extends from the outer radius of the central opening to the inner radius of the larger vessel and is referred to as the acceleration stage. A large azimuthal current, labeled J_{Coil} in Fig. 1, is quickly pulsed through the coil. For a high-enough current rise rate,[5] dI/d$t \geq 10^{10}$ A/s, this pulse induces a current sheet in the plasma, which initially forms parallel and very close to the backend.
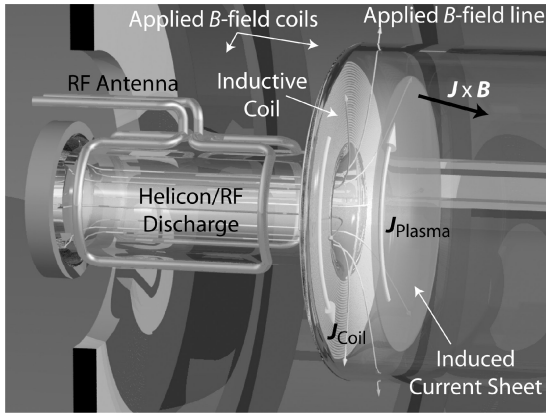
Fig. 1 Schematic illustration of the FARAD concept.

The current sheet, shown as a thin disk in the figure, contains an induced azimuthal current, labeled J_{Plasma}, which flows in the opposite direction to the current in the coil. The induced current density interacts with the magnetic fields resulting in a Lorentz body force density.

B. Motivation

The FARAD concept shares one main feature with a previous concept, namely, the pulsed inductive thruster (PIT).[6−8] That feature is the inductive production and acceleration of a current sheet via a current pulse in an external coil. As such, we expect the propulsive characteristics of an optimized FARAD thruster to be quite comparable to the PIT ($I_{\mathrm{sp}} = 2000–8000$ s, $\eta_t = 40–50\%$).

The novelty of the FARAD is that the plasma is preionized by a mechanism separate from that used to form the current sheet and accelerate the gas. This is much different than that in the PIT, where ionization, current sheet formation, and acceleration are all performed by the pulse of current flowing through the acceleration coil. An additional conceptual difference between the FARAD and the PIT is that in the FARAD the propellant is fed as a plasma from upstream of the acceleration stage instead of as a neutral gas fed from downstream by a sizable nozzle.

We show in this paper that using a separate preionization mechanism, such as the one found in our experiment, allows for the formation of an inductive current sheet at much lower discharge energies and voltages than those used in the PIT, even though our proof-of-concept experiment is poorly optimized for inductive current sheet formation and acceleration. Although the experimental data contained in this paper were obtained at discharge energies of 78.5 J/pulse, inductive current sheets have been formed in the proof-of-concept experiment at energies as low as 44 J/pulse (vs 4 kJ/pulse in the PIT). Relief of the high-energy, high initial voltage design constraint on pulsed inductive current sheet formation has the potential to lead to smaller, more compact thrusters for spacecraft systems.

In addition to the acceleration produced by the interaction of the induced magnetic field and plasma current, an additional acceleration component can be realized through the interaction of the applied magnetic field with the induced current. However, a strong applied magnetic field can impede the azimuthal current in the sheet, thus lowering thruster efficiency. Study of this aspect of the FARAD is beyond the scope of this paper, but we mention it here as it merits separate investigation.

The outline for the rest of the paper is as follows. In Sec. II the FARAD proof-of-concept experiment is described while the diagnostics employed are briefly described in Sec. III. Data demonstrating the concept of low-voltage, low-energy pulsed inductive acceleration are presented in Sec. IV and discussed in greater detail in Sec. V.

II. FARAD Proof-of-Concept Experiment

The different components of the FARAD proof-of-concept experiment are described next. These components are assembled to form the dedicated experimental facility shown in Fig. 2.
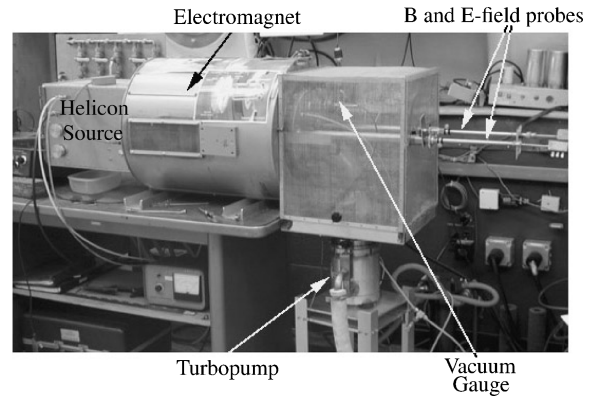

Fig. 2 Photograph of the facility used for the FARAD proof-of-concept experiment. The picture shows the water-cooled electromagnet, Faraday cage, turbopump, and associated equipment. The plasma helicon source is located inside the box on the left-hand side.
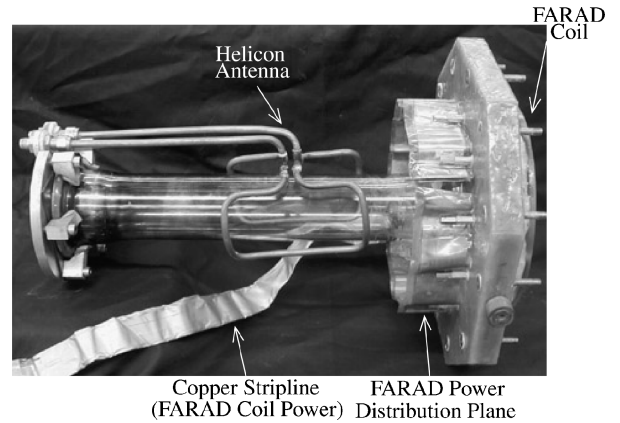

Fig. 3 Side view of the fully assembled FARAD proof-of-concept experiment. This photograph can be compared directly to the conceptual schematic shown in Fig. 1.

A. Vacuum Vessel

The vacuum vessel consists of two Pyrex cylinders placed inside of an electromagnet. The small cylinder has a 6-cm inner diameter and is 37 cm in length while the large cylinder has a 20-cm inner diameter and is 46 cm in length. The cylinders are connected using a G-11 (fiberglass) plate with a 6-cm concentric hole at the center to allow free flow of gas between the two cylinders. A flat induction coil (used to accelerate the plasma) is mounted to the G-11 plate inside the vacuum chamber. A photograph of the small cylinder mated to the G-11 plate is shown in Fig. 3.

A constant background pressure (0.1 to 55 mtorr) can be maintained by a gas feed located at the endplate of the large cylinder and by a 150 l/s turbo pump with a conductance controller backed by a roughing pump. A background pressure of 5×10^{-6} torr can be maintained while the turbopump is operating and the conductance controller is in the open position.

B. Applied Magnetic Field

The applied magnetic field is generated using a Varian VA-1955A klystron magnet. (No effort at this proof-of-concept stage has been made to develop a compact magnet that would be more ideal for an actual thruster.) This apparatus contains five separate, water-cooled magnet coils (see schematic in Fig. 4). The magnet wiring has been altered to allow the currents in coils 1 and 2 and coils 3, 4, and 5 to be driven in opposite directions by two different power supplies. Using two electronic measurements EMCC 120-40 power supplies to drive the current in opposite directions in these coil sets, a cusped magnetic field can be created.

1. Magnetostatic Modeling

A two-dimensional axisymmetric numerical model of the magnet and case is constructed and solved using a magnetostatic modeling program (Maxwell SV, Ansoft Corporation). The model is shown to scale in Fig. 4. Each coil set consists of three separate, concentric, toroidal copper rings. Each ring carries an equal amount of the total assigned current. The magnet casing is modeled with a relative magnetic permeability of 60. As in the experiment, the currents in coil sets 1 and 2 flow in the same direction, while coil sets 3, 4, and 5 are driven by a separate power supply in the opposite direction. Throughout this paper, the axial position $z = 0$ is coincident with the location of the acceleration coil.

2. Applied Field Measurements

Measurements of the steady-state magnetic field in the coil were performed using an FW Bell gaussmeter (model 5080) calibrated to an accuracy of 1%. The axial and radial components of the field were measured on a grid with spacings in both the axial and radial directions of 1.27 cm ($\frac{1}{2}$ in.). This grid covers 10.16 cm (4 in.) in the radial direction and 58.42 cm (23 in.) in the axial direction. The current provided by the power supply for coils 1 and 2 was 23.9 A, whereas the current for coils 3, 4, and 5 was

10.2 A (e.g., total current assigned to coil set #1 = 23.9 A × 182 turns = 4350 A-turns). The results of the applied field measurement are given in the top half of Fig. 5 while the bottom half of the same figure shows results predicted by the magnetostatic model operating under the same conditions. The agreement with the model is excellent as the calculated and measured maps are practically indistinguishable.

The magnetostatic model is used to find values for the current in each coil that would yield a mostly radial field at the coil face while still producing a mostly axial field in the helicon stage. For the given configuration, there is a wide range of current values for which an axial field is produced in the helicon stage. Plots of the magnetic field lines are used to identify field geometries that could deliver magnetized particles from the inductive discharge to the acceleration coil face. Although a cusp magnetic field is produced in the proof-of-concept experiment, it is only an artifact of how the applied magnetic field is presently generated. Only the axial field in the helicon stage and the mostly radial field in the acceleration stage are truly necessary. In a real thruster, the radial field should have some finite value at the coil face and then drop quickly to near zero over a distance that is shorter than the acceleration length scale, helping to guarantee magnetic field detachment. Such a field geometry could be constructed using a combination of Helmholtz coils and magnetic pole pieces.

C. Plasma Generation

A Boswell-type saddle antenna (helicon antenna)[9] is placed around the small cylinder (shown on the left side of Fig. 3) and used to generate the plasma. The antenna is constructed of copper tubing to allow water cooling during operation. The helicon discharge[2–4] is produced by supplying power (steady-state or pulsed) to the antenna from an ENI 13.56 MHz, 1.2-kW power supply through a tuner. The tuner consists of an L network composed of two Jennings 1000 pF, 3-kV variable vacuum capacitors. It is located as close to the antenna as possible to maximize coupling efficiency.

At the power levels we operated the plasma source (500 W and above), the measured plasma density, electron density, electron temperature, reflected powers[10] as well as the luminous structure of the plasma inside the source (a bright pencil-like core of bright emission surrounded by a plasma) all correspond to what is commonly described as a helicon source in the literature (see Ref. 3 and the
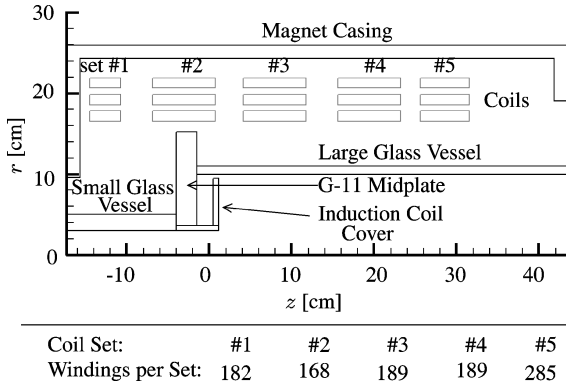

Coil Set:	#1	#2	#3	#4	#5
Windings per Set:	182	168	189	189	285

Fig. 4 Axisymmetric schematic depicting the geometry of the magnet and vacuum vessel (to scale). The acceleration coil is located at $z = 0$ in all of the plots in this paper.
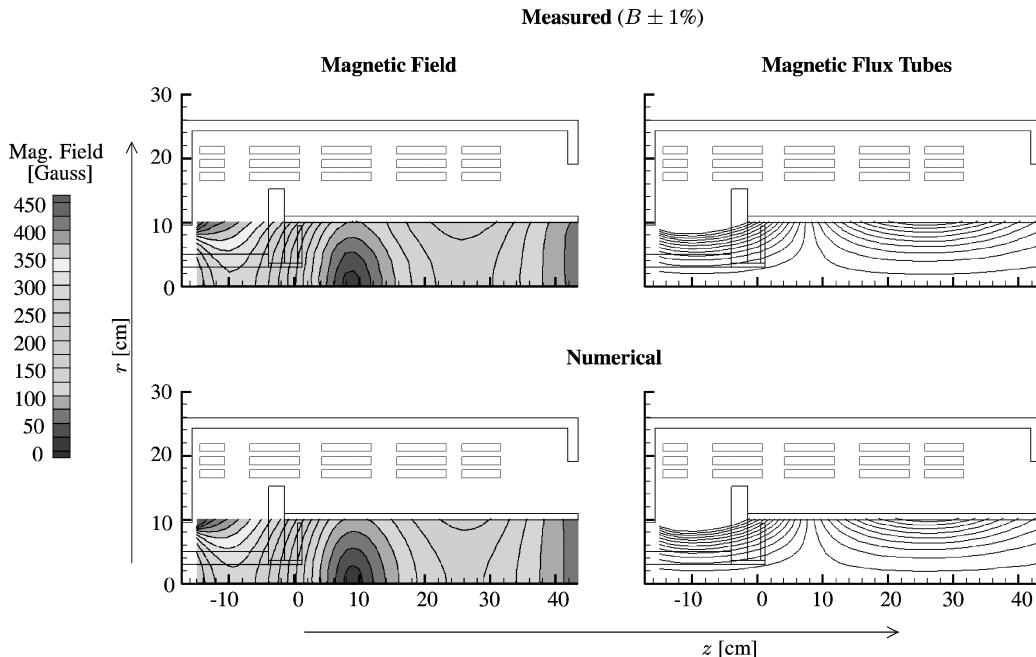

Fig. 5 Applied magnetic field measurements (top) and modeling results (bottom) for the calibration case where the current in coils 1–2 is 23.9 A and the current in coils 3–5 is 10.2 A, showing excellent agreement.

references within) as opposed to an inductive discharge. Although the axial field strength in the small cylinder is approximately 400 G for the data contained in this paper, helicon discharges were ignited at field strengths of 175–200 G.

D. Acceleration Coil

The FARAD acceleration coil (seen in Fig. 6) is similar to the Marx-type coil used by Lovberg and Dailey in later generations of the PIT.[7] However, it is quite different in scale and pulse energy. The PIT MkV coil is composed of 18 half-turn coils, has an outer diameter of 1 m, and operates at roughly 4 kJ/pulse. The FARAD proof-of-concept experiment, on the other hand, possesses 12 half-turn coils, has an inner diameter of 20 cm, and has been operated from 44 to 78.5 J/pulse.

The half-turn coils are connected in parallel using copper strips. A 39.2-μF capacitor is remotely located and connected to the coil using copper stripline. Current is switched using a simple contact, or "hammer," switch. In a real thruster, SCRs or some other type of solid-state switching would be used. A lumped-element circuit schematic of the acceleration stage, showing both the driver circuit and the inductively coupled plasma, is shown in Fig. 7. The external circuit possesses capacitance C, external inductance L_0, resistance R_e, and acceleration coil's inductance L_C. The plasma also has an inductance equal to L_C and a resistance R_p. The two circuits are inductively coupled through the acceleration coil, which acts as a transformer with mutual inductance M.

In a real thruster, one would want the fractional change in inductance to be high ($\Delta L/L_0 > 1$). In our experiment, though, $\Delta L/L_0 \approx 15\%$. This is an unfortunate effect of adopting the PIT's half-turn Marx-type coil geometry, which possesses a low inductance at small diameters. However, demonstrating current sheet formation and *any* subsequent acceleration in this unoptimized configuration serves to demonstrate the robustness of the concept. The coil's inductance can be increased in later generations of the FARAD by using multiple-turn spiral coils.
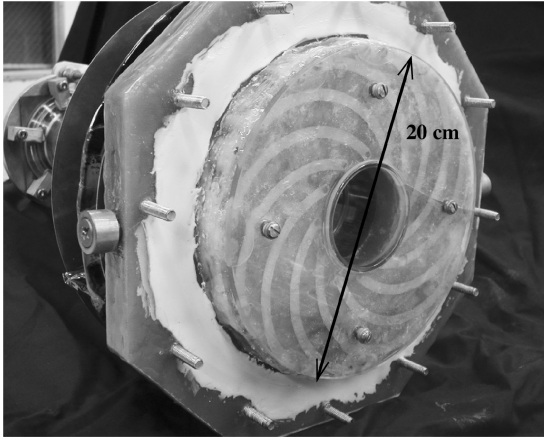

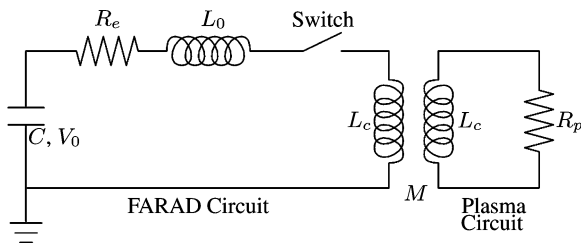**Fig. 6   Skewed-end view of the fully assembled FARAD experiment showing the face of the acceleration coil.**

Fig. 7   Circuit schematic of the FARAD acceleration coil and the inductively coupled plasma.

E. Experimental Operation

During operation of the FARAD proof-of-concept experiment, a helicon plasma is initiated and allowed to reach a steady-state condition. The duration of the helicon discharge prior to pulsing the acceleration coil is ~1–2 s. The helicon source remains active well after the acceleration pulse [$\mathcal{O}(1–10)\ \mu$s] is complete.

Thruster pulsing scheme: We note here that, in a real thruster, care should be taken in choosing the correct pulse widths and the interpulsing scheme. There are three major pulsed systems in the FARAD concept (the applied B-field being left in a steady-state mode for this discussion):

1) The neutral gas pulse, of temporal extent Δt_g, precedes the other pulses and should be long enough to fill the helicon stage with neutral gas but short enough to avoid leaking gas to the second (acceleration) stage.

2) The rf pulse length Δt_{RF} is the duration that power is supplied to the helicon stage. Although the helicon stage can be operated in a steady-state mode (as we have done in the proof-of-concept experiment), it must be operated in a pulsed mode in a real thruster because the acceleration mechanism itself is pulse. In a real thruster the rf pulse is not started until the injected gas has filled the helicon stage and must end late enough to allow most of the produced plasma to migrate to the backend of the acceleration stage but early enough to avoid producing extraneous plasma that cannot participate in the acceleration process.

3) The acceleration coil pulse Δt_a must not start until most of the plasma has been guided to the backend of the acceleration stage and must not end until the current sheet has traveled an axial distance z_{emc}, which represents the axial extent of the region (measured from the backend) in which electromagnetic coupling between the sheet and the coil occurs. For axial locations $z \geq z_{emc}$ the current sheet is decoupled from the acceleration coil.

The demand for a fast gas valve can be alleviated by employing a burst-pulse scheme similar to that developed for gas-fed pulsed plasma thrusters.[11,12] In this mode, a "slow" and sturdy valve is operated at a low duty cycle, and the thruster is operated in a burst of discharge pulses, with a Δt between each consecutive *pulse* equal to the time it takes the current sheet to sweep the gas through the thruster. The time between the *bursts* is dictated by the available steady-state power and the required (average) thrust. If the response time of the rf-matching network is too slow to switch the preionization pulse on and off for each individual acceleration pulse, it too can operate at the lower duty cycle associated with the slow valve.

Optimization of the pulsed systems is beyond the scope of the proof-of-concept experiment because an ambient fill technique and steady-state rf discharge were used. However, it is clear that the pulse intersequencing and relative magnitudes of Δt_g, Δt_{RF}, and Δt_a will have significant impact on both the mass utilization efficiency and the propulsive performance of a real thruster and require further investigation.

III.   Diagnostics

A.   Current Monitoring

The current flowing through the acceleration coil J_{Coil} is monitored using an air-core Rogowski coil.[13] The raw probe output, which is proportional to the derivative of the enclosed current, is integrated numerically to yield a current waveform. The error on the calibration constant, which multiplies the integrated Rogowski coil waveform, is ±3%, and the numerical integration errors have been estimated to add an additional 2% error for a total of ±5%.

B.   Induced Magnetic Field

The induced (time-varying) magnetic field measurements are acquired using B-dot probes.[14] Three Panasonic 220-nH wire-wound nonmagnetic core surface mount inductors are used to measure dB/dt in three orthogonal directions in a manner similar to that found in Ref. 15. The probe head is contained within a glass tube that protects it from the plasma. The tube diameter is on the order of millimeters, so as to not significantly disturb the plasma. The numerically integrated dB/dt signals are multiplied by their respective
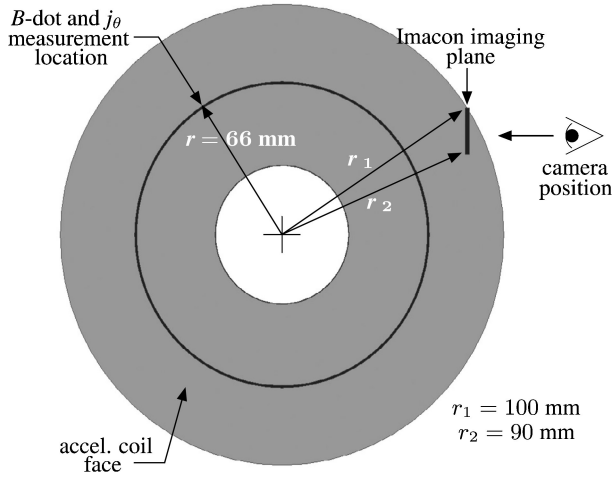
Fig. 8   Schematic showing the relative locations of 1) the magnetic field probe data and 2) the plane imaged by the fast-framing Imacon camera. The schematic is to scale, and the vertical extent of the imaging plane matches the extent of the images presented in this paper.

calibration constants and linearly combined to obtain $B(t)$ in the r-θ-z coordinate system. The error on the measurement of B_r is $\pm 5\%$. The radial location for our measurements is given schematically in Fig. 8.

C.   Current Sheet Visualization

Visualization of current sheet formation and its subsequent motion is accomplished using a Hadland Photonics Imacon 792/LC fast-framing camera. The photographs are obtained using a 20 million frames per second module, with each frame having an exposure time of 10 ns. Because of obstructions in the optical path, only one region of the plasma, located on the face of the acceleration coil and extending 20 mm in the vertical direction, is imaged. A mask is affixed to the outside of the vacuum vessel to allow the current sheet's absolute position to be determined in each exposure. Consequently, the imaging plane is located at the edge of the vacuum vessel to properly image the mask (see Fig. 8 for the relative location of the imaging plane). The photographs are obtained without filtering, and so any light emission that is bright enough to be imaged is seen. However, the rf/helicon plasma that reaches the acceleration coil face did not produce enough light on its own to appear in any of our photographs, and so we assume that the light captured in each exposure corresponds to emission from the current sheet.

IV.   Experimental Data

In this section, data that demonstrate the formation of a low-energy, low-voltage current sheet are presented. In addition, the sheet experiences significant acceleration during the first half-cycle of the discharge. The working gas for these data is argon at 23 mtorr (in both the helicon and acceleration stages). The chamber is first evacuated, and then a uniform fill technique is used to introduce the gas. The pressure is chosen because the strongest current sheet (determined using magnetic field traces, fast-framing photography, and naked-eye observations) forms at this pressure. The helicon is operated at 1000 W of forward power, but operation down to 500 W results in insignificant changes in the magnetic field waveforms and photographic images.

A.   Visual Observations

Simple visual observations provided verification of the passive magnetic-field-guided plasma injection onto the acceleration coil face. The helicon plasma is quite luminescent and can be seen following the applied magnetic field lines and spreading over the acceleration coil (see Fig. 9). The luminosity is greatest at the centerline of the device and decreases with increasing radius. This is not surprising because we expect that the initial, preionized plasma density scales like $1/r$ as the plasma spreads radially outward across the ac-
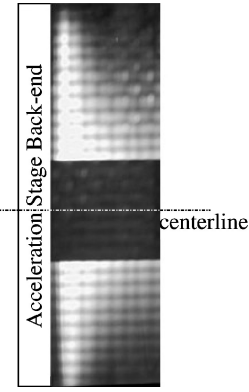

Fig. 9   Photograph of the steady-state rf plasma as it follows magnetic field lines and spreads out over the face of the acceleration coil (viewed through a 1.0 neutral density filter). The bright area adjacent to the backend, where the acceleration coil is located, is emission from the injected plasma. The grid pattern in the picture is because of the mesh of the Faraday cage enclosing the experiment and the dark, rectangular shape near the centerline is a structural member outside the chamber.
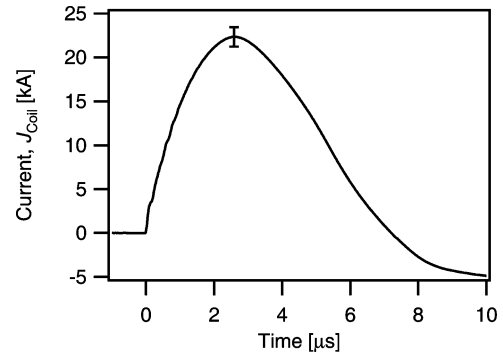

Fig. 10   Total current in the acceleration coil J_{Coil} (with a typical error bar) for a pulse energy of 78.5 J.

celerator coil face. In the current configuration, a great deal of the plasma stays anchored alone the centerline and is not turned. This issue would have to be addressed in a real thruster. Also, the plasma density in a real thruster, while being greatest near the centerline, must be of a sufficient magnitude at the outside edge of the coil to allow for low voltage current sheet to form over the entire coil face.

Visual observations provide evidence of current sheet formation. When current is pulsed through the acceleration coil, a very bright "flash" of light appears in a thin region near the coil. The flash appears homogeneous over the face of the coil, and its intensity temporarily overwhelms the light emitted by the steady-state (helicon) plasma. The short-duration, bright light emission is indicative of increased ionization caused by current sheet formation across the coil face. Although these observations are only qualitative, no current sheet formation was observed when the preionized plasma was not present. This leads to the conclusion that our configuration directed "enough" preionized plasma to the acceleration coil face to allow for the formation of a current sheet at low discharge energies.

B.   Coil Current

A typical driver circuit current waveform is given in Fig. 10. Because the fractional change in the inductance is low, the coil current is roughly the same with or without a current sheet present. The maximum dJ_{Coil}/dt in our circuit is roughly 1.8×10^{10} A/s, which is on the order of the level required to form a current sheet.[5]

C.   Magnetic Field

1.   Applied Field

Values of the applied (steady-state) magnetic field are computed numerically using the magnetostatic model presented in Sec. II.B. For completeness, plots of the variation of the applied field (B_r and
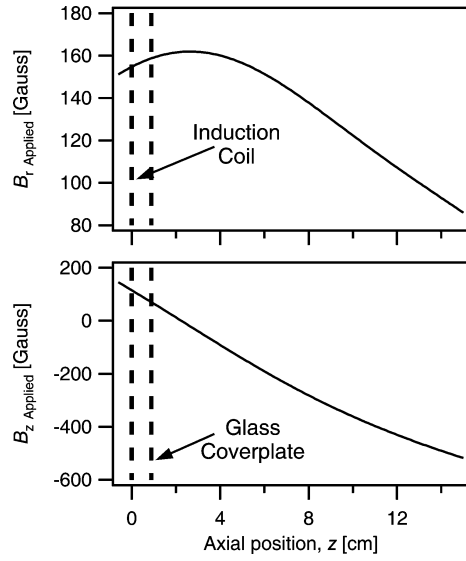
Fig. 11   Calculated applied magnetic field strengths in the r and z directions in front of the acceleration coil at a radius of 66 mm. The coil position ($z = 0$) and the location of the surface of the glass plate covering the coil are sketched in the plot.

B_z) along an axial line at a radius of 66 mm are given in Fig. 11. In the model, coils 1–2 are supplied with 38 A, whereas 36.5 A are delivered to coils 3–5 by the power supply. These currents match those used during the experimental trials. The B_r field peaks just in front of the coil while the B_z field at that location goes to zero, as expected.

The magnitude of the applied field and a rough measure of the number density at the coil face before the pulse (found as 10^{11} cm^{-3} using an rf-compensated Langmuir probe[16]) can be used to compute the electron and ion Hall parameters and the collisional mean free paths in the experiment before the pulse. The calculations reveal that the electrons are partially magnetized ($\omega_{ce}/\nu_{ei} \gg 1$, electron-neutral mean free path on the order of centimeters), but the ions are not ($\omega_{ci}/\nu_{ii} \ll 1$). (Note that some ions can be turned by microscopic polarization fields forming as the more mobile electrons turn along the field lines and race towards the outer edge of the acceleration coil.) Although this is acceptable for our proof-of-concept experiment, the ions in a real thruster would have to be turned by either a much stronger applied field or some type of duct or nozzle to avoid a low mass utilization efficiency.

2. Induced Field

Data showing the temporal and spatial variation of the induced radial field acquired at a radius of 66 mm are presented in Fig. 12. The axial z locations are evenly spaced every 5 mm between 1.3 and 5.3 cm from the coil face. We see first that the induced field strength is stronger than the applied magnetic field, temporarily overwhelming the latter's effect on the plasma during the pulse. Notice that the traces all begin increasing immediately at $t = 0$. This feature has been previously observed in pulsed inductive devices[6,17] and indicates that the initial fields induced by the coil rapidly diffuse through the plasma, implying low initial conductivity. At a time shortly after $t = 0$, the waveforms exhibit a distinct "knee," or inflection point. This knee is indicative of current sheet formation and the associated increases in plasma conductivity and electromagnetic shielding that accompany it. The field emanating from the current sheet propagates at the speed of light through the weakly ionized downstream portion of the plasma causing all of the knees to appear coincident (or very nearly so) in time.

3. Current Density

Magnetic field maps, like those presented in Fig. 12, provide a good qualitative indication of the presence and effect of a current
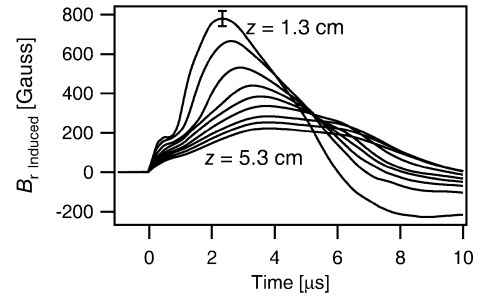

Fig. 12   Time histories of the induced radial magnetic field strengths (with a typical error bar) at various axial stations at a radius of 66 mm. The axial positions are spaced evenly every 5 mm. The discharge energy was 78.5 J, and the background pressure was 23 mtorr.
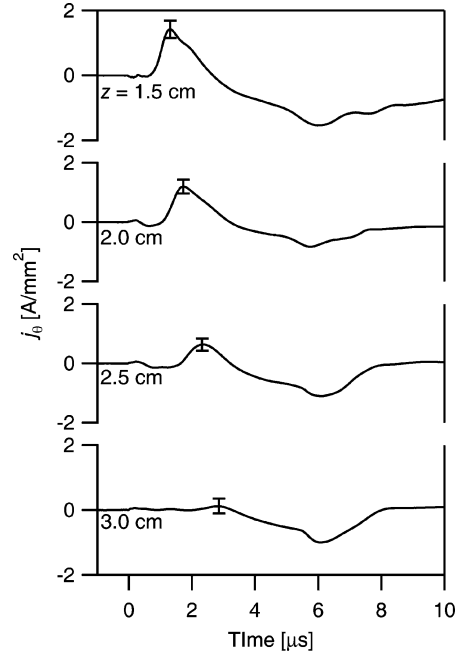

Fig. 13   Time histories of the induced plasma current densities (with typical error bars) at various axial stations at a radius of 66 mm. The axial positions are spaced evenly every 5 mm. The discharge energy was 78.5 J, and the background pressure was 23 mtorr.

sheet. However, as the induced magnetic field is a linear superposition of two separate current sources, the current in the coil and the induced current sheet, there is a great deal of ambiguity involved in the interpretation of field data acquired along a single, axial line. This difficulty is bypassed by measuring the magnetic field in a two-dimensional r-z plane and using Ampère's law,

$$\nabla \times \boldsymbol{B} = \mu_0 \boldsymbol{j}$$

to compute the current density j_θ in the sheet. This works because the only portion of the magnetic field in the region of interest that is not curl free is attributable to the current sheet.

Azimuthal current density profiles in the FARAD experiment are presented in Fig. 13. To numerically compute the curl of B, data on a two-dimensional, r-z grid are required. The axial spacing Δz between the magnetic field data points is 5 mm, and the radial spacing Δr is 4 mm straddling $r = 66$ mm. The error bars are a combination of the errors on the magnetic field measurements and the uncertainty on the B-dot probe positions.

The initial peak in the current density profile at each axial station represents the current sheet. We observe a weakening of the sheet as it reaches axial stations located further away from the acceleration coil. The current sheet velocity can be estimated based upon

the time the peak current passes the different axial stations. The inferred current sheet velocity between $z = 1.5$ and 2.0 cm is 12 km/s, whereas the velocity between $z = 2.0$ and 2.5 cm is 8 km/s.

The induced current in the plasma goes to zero when the current in the external circuit is maximum (see Fig. 10). Also, the azimuthal current at every displayed axial station turns negative once the coil current passes through its maximum, that is, when dJ_{Coil}/dt changes sign producing a weak induced azimuthal current throughout the entire volume. We conclude that the formation of an inductive current sheet must possess some minimum threshold dJ_{Coil}/dt value, and in our experiment this threshold is not attained when the external current pulse reverses.

D. Current Sheet Visualization

A track of the current sheet position is presented in Fig. 14, whereas representative photographs of the current sheet at several instances in time are presented in Fig. 15. The current sheet locations found in Fig. 14 are determined as follows. Digitized frames are loaded into a program capable of performing image processing operations (Igor Pro, Wavemetrics, Inc.). The intensity values of individual pixels are summed in the vertical r, direction yielding a waveform composed of summed intensity as a function of z. A
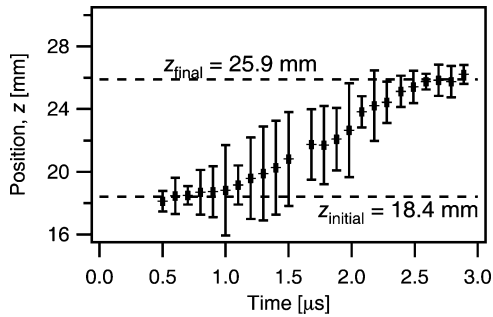

Fig. 14 Current sheet position history obtained using the fast-framing camera. Error bars show the width of the Gaussian fit to the luminous portion of the discharge. The discharge energy was 78.5 J, and the background pressure was 23 mtorr.

Gaussian distribution is then fit to the intensity waveform,

$$\text{Intensity} = A \exp\left\{-\left[(z - z_0)\big/\sqrt{2}\sigma\right]^2\right\}$$

where A is a constant, z_0 is taken to be the current, sheet center, and σ is taken as a measure of the error on z_0.

The track (Fig. 14) clearly shows three separate phases in the discharge; initiation, acceleration, and termination. The images presented in Fig. 15 are meant to be representative of the discharge and will aid in our interpretation of the photographic data. (Note that although the images in Fig. 15 were contrast enhanced, the raw images analyzed in the production of Fig. 14 were not enhanced.) The current sheet initiates at $z = 18.4$ mm and remains stationary, with its light emission increasing and intensifying until $t \approx 1.1$ μs. It then quickly accelerates, reaching a constant velocity, which it maintains between 1.1 and 2.4 μs. A linear curve fit of this portion of the data yields a sheet speed of approximately 4.6 km/s. Finally, between 2.4 and 3 μs, the current sheet's motion ceases, and its light emission decreases. The termination phase occurs as dJ_{Coil}/dt in the external circuit approaches zero, mirroring the result of the current density measurement.

V. Discussion

Our measurements clearly indicate that the preionized plasma couples with the current in the acceleration coil to further ionize the gas and form a current sheet. The delay between when the coil current is pulsed and when the current sheet forms poses a serious efficiency problem for a real pulsed inductive accelerator as magnetic field energy, which could perform work, is instead radiated into free space. Although we encounter this problem in our proof-of-concept experiment, we expect that increasing the initial current rise rate in the coil, which can be done by lowering the parasitic inductance L_0, will help in minimizing the time between pulse initiation and current sheet formation as it did in Ref. 6.

The measurements of the induced magnetic field and azimuthal current density (referred to as the field measurements throughout this discussion) compare quite well with the current sheet visualization and analysis (referred to hereafter as the optical measurements). Both measurements indicate that, after an initial delay, a current sheet forms and moves a finite distance. Because the coil's

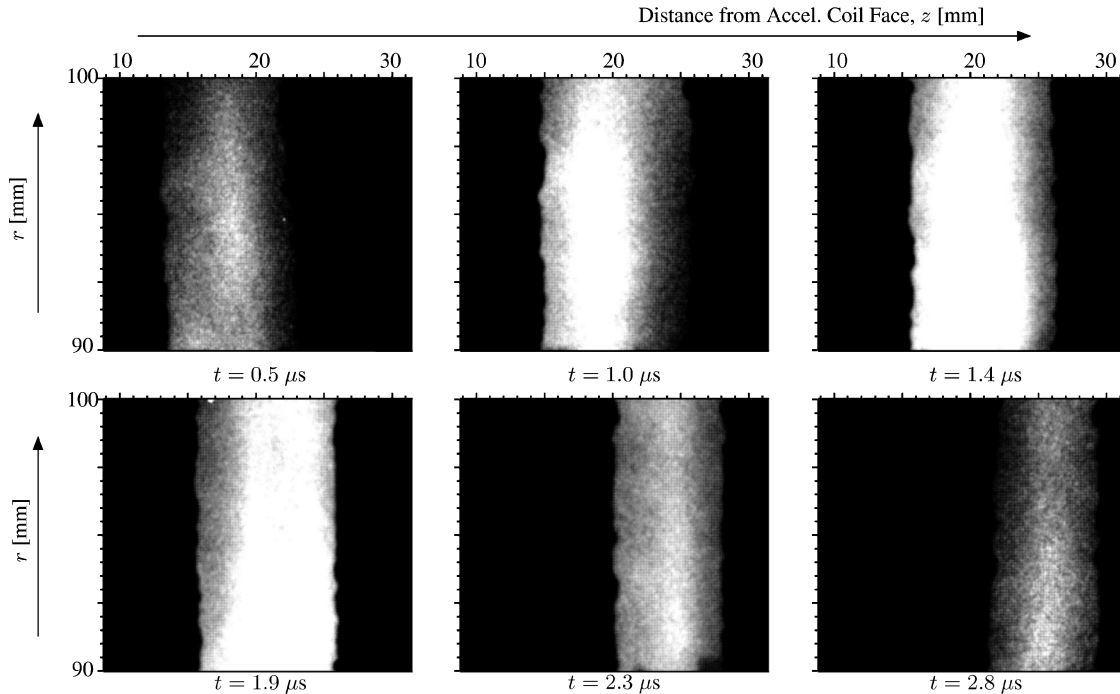Distance from Accel. Coil Face, z [mm]

Fig. 15 Representative high-speed photographs acquired using a fast-framing camera at a framing rate of 20 million frames per second. These photos show the sheet initiation ($t = 0.5$ μs), acceleration ($t = 1.0$ to 2.3 μs) and termination ($t = 2.8$ μs). (The contrast in these photographs has been enhanced through digital image processing.)

inductance, and consequently the mutual inductance M, between the coil and the sheet are relatively small in the experiment, the plasma sheet dynamics are effectively driven only by dJ_{Coil}/dt. Consequently, the sheet terminates as dJ_{Coil}/dt approaches zero. Increasing the coil inductance in a real thruster will result in a current sheet with longer lifetime that also experiences additional acceleration (both processes are driven by dJ_{Coil}/dt and dM/dt).

There are, however, two apparent discrepancies between the field and optical measurements. Examination of these apparent discrepancies leads to additional physical insight into the current sheet evolution.

The first discrepancy is the difference between the sheet velocity (12 km/s) obtained from the magnetic field probe data and that (4.6 km/s) inferred from the photographs in Fig. 15. This discrepancy can be qualitatively explained in light of the observed induced magnetic field gradient $\partial B_r/\partial r$, which implies a weakening of the induced magnetic field, and thus a lowering of the sheet velocity, at the outer radial location (90–100 mm) where the photographic observations were obtained, as compared to the radial location ($r = 66$ mm) where the magnetic probe measurements were made.

The second discrepancy is the difference between the axial positions of the current sheet when determined optically and from the probe data at a given time. For instance, at $t \approx 1.4$ μs the sheet axial position is observed optically to be at about $z \approx 20$ mm from the backplate (Fig. 15) while the probe data (Fig. 13) give $z \approx 15$ mm. This can be explained by first noting from Fig. 11 that the applied magnetic field lines in the acceleration stage are not purely radial but are in fact tilted by about 20 deg with respect to the backplate. This canting of the applied magnetic field should be expected to lead to a canted current sheet when the latter is initially formed. It is therefore not surprising that the initial axial position of the sheet at outer radii (where the optical measurements were made) leads the axial location of the sheet at inner radii (where the probe is located). The radially decreasing axial sheet velocity discussed in the preceding paragraph compensates somewhat for this initial canting as the sheet evolves in time.

Triple probe measurements were unsuccessfully attempted in this experiment. We believe these measurements were unsuccessful for two reasons. The first is that no power supply with a fast enough response time was available for use in our experiment. The second is that many of the assumptions made in Langmuir and triple probe theory (specifically that the plasma is nonmagnetized and the sheath is collisionless) are violated during the discharge pulse. Using the laser interferometry system described in Ref. 18, we were able to measure the maximum plasma density as roughly 7×10^{14} cm^{-3}. However, this density is at the very edge of that system's resolution, so that no further time-resolved measurements could be attained.

One can wonder if the current sheet is actually accelerating any mass. Because no thrust stand measurements were performed, this is a valid concern. If the entire fill density were accelerated by the $\boldsymbol{j} \times \boldsymbol{B}$ body force [$j_\theta = \mathcal{O}(1 \text{ MA/m}^2)$, $B_r = 0.06$ T, $\rho_0 = 5 \times 10^{-5}$ kg/m^3, $t = \mathcal{O}(1 \text{ }\mu s)$], it would only reach a speed on the order of 1 km/s. However, this assumes that the sheet perfectly entrains all of the mass available to it. Research in pulsed plasma thrusters has shown that the current sheet is, in fact, permeable, and a certain amount of gas can slip behind the sheet.[19] One way to infer whether mass is accelerated is to compute the electron-ion momentum exchange coulomb mean free path. If we take $n_e = \mathcal{O}(10^{14}$ cm$^{-3})$ and $T_e = 2.5$ eV, then the mean free path is 1–2 mm, implying significant momentum coupling between the electron and ion fluids on the length scale of the observed motion. Moreover, the luminous front, which can only be emission from excited argon ion states, is not merely the result of an ionization front going through the gas, but a manifestation of a current sheet entraining at least some ions that are coupled to the electrons by momentum-exchange collisions (which on a macroscopic scale is equivalent to a neutral plasma gaining acceleration via a $\boldsymbol{j} \times \boldsymbol{B}$ body force).

VI.   Conclusions

We have presented a new rf-assisted pulsed inductive accelerator concept, FARAD, and presented the results from a proof-of-concept

experiment aimed at demonstrating the principle of low-energy, low-voltage inductive current sheet formation. The following conclusions can be made:

1) Partially decoupling the ionization and acceleration processes through the use of a separate preionization mechanism in the FARAD allowed for current sheet formation at substantially lower discharge voltages and energies than previous pulsed inductive accelerator concepts (44 J/pulse as opposed to 4 kJ/pulse in the PIT).

2) Visual observations in the proof-of-concept experiment indicate that preionized plasma follows magnetic field lines and forms a plasma slab on the face of the acceleration coil. Also, when current is pulsed through the acceleration coil, a bright flash on the coil surface is visible to the naked eye, indicative of increased ionization associated with current sheet formation.

3) Magnetic field probing gives qualitative evidence of the presence and effect of a current sheet. The curl of the induced magnetic field yields a direct measure of the current density profile at different axial stations within the acceleration stage. A peak sheet speed of 12 km/s is inferred from that data.

4) Visualization using a fast-framing camera provides an observation of the formation of the current sheet and its subsequent acceleration.

5) There are discrepancies in the sheet speed inferred from the magnetic field measurements and that found using photography (though both inferred speeds are of the same order). However, these discrepancies should be expected because the magnetic field probing and photographic measurements are obtained at different radial locations possessing different induced field strengths.

6) Because of the finite axial component of the applied magnetic field in the acceleration stage, the current sheet, which forms at the location of the preionized plasma following the applied field lines, is initially canted forward at larger radii. This canting is alleviated as the sheet accelerates to higher velocities at lower radii as a result of an induced magnetic field that decreases with increasing radius.

References

[1]Choueiri, E. Y., and Polzin, K. A., "Faraday Acceleration with Radio-Frequency Assisted Discharge (FARAD)," AIAA Paper 2004-3940, July 2004.

[2]Chen, F. F., and Boswell, R. W., "Helicons—The Past Decade," *IEEE Transactions on Plasma Science*, Vol. 25, No. 6, 1997, p. 1245.

[3]Boswell, R. W., and Chen, F. F., "Helicons—The Early Years," *IEEE Transactions on Plasma Science*, Vol. 25, No. 6, 1997, p. 1229.

[4]Lehane, J. A., and Thonemann, P. C., "An Experimental Study of Helicon Wave Propagation in Gaseous Plasma," *Proceedings of the Physical Society*, Vol. 85, No. 2, 1965, p. 301.

[5]Jahn, R. G., *Physics of Electric Propulsion*, McGraw–Hill, New York, 1968, p. 286.

[6]Dailey, C. L., and Lovberg, R. H., "PIT Clamped Discharge Evolution," TRW Space and Technology Group, Technical Rept., AFOSR-TR-89-0130, Redondo Beach, CA, Dec. 1988.

[7]Dailey, C. L., and Lovberg, R. H., "The PIT MkV Pulsed Inductive Thruster," TRW Systems Group, Technical Rept., NASA CR-191155, Redondo Beach, CA, July 1993.

[8]Dailey, C. L., and Lovberg, R. H., "Current Sheet Structure in an Inductive-Impulsive Plasma Accelerator," *AIAA Journal*, Vol. 10, No. 2, 1972, pp. 125–129.

[9]Ellingboe, A. R., Boswell, R. W., Booth, J. P., and Sadeghi, N., "Electron Beam Pulses Produced by Helicon-Wave Excitations," *Physics of Plasmas*, Vol. 2, No. 6, 1995, p. 1807.

[10]Spektor, R., and Choueiri, E. Y., "Excitation and Propagation of Electrostatic Ion Cyclotron Waves in rf-Sustained Plasmas of Interest to Propulsion Research," AIAA Paper 2004-4095, July 2004.

[11]Ziemer, J. K., Cubbin, E. A., Choueiri, E. Y., and Birx, D., "Performance Characterization of a High Efficiency Gas-Fed Pulsed Plasma Thruster," AIAA Paper 97-2925, July 1997.

[12]Ziemer, J. K., Choueiri, E. Y., and Birx, D., "Trends in Performance Improvements of a Gas-Fed Pulsed Plasma Thruster," International Electric Propulsion Conf., Paper 97-040, Aug. 1997.

[13]Wright, E. S., "The Design and Development of Rogowski Coil Probes for Measurement of Current Density Distribution in a Plasma Pinch," Dept. of Aerospace and Mechanical Sciences, Princeton Univ., Rept. 740, Princeton, NJ, June 1965; also M.S.E. Thesis, May 1965.

[14]Lovberg, R. H., "Magnetic Probes," *Plasma Diagnostic Techniques*, edited by R. H. Huddlestone and S. L. Leonard, Academic Press, New York, 1965, pp. 69–112.

[15]Romero-Talamás, C. A., Bellan, P. M., and Hsu, S. C., "Multielement Magnetic Probe Using Commercial Chip Inductors," *Review of Scientific Instruments*, Vol. 75, No. 8, 2004, p. 2664.

[16]Sudit, R., and Chen, F. F., "RF Compensated Probes for High-Density Discharges," *Plasma Sources Science and Technology*, Vol. 3, No. 2, 1994, pp. 162–168.

[17]Lovberg, R. H., and Dailey, C. L., "Current Sheet Development in a Pulsed Inductive Thruster," AIAA Paper 89-2266, July 1989.

[18]Markusic, T. E., "Current Sheet Canting in Pulsed Electromagnetic Accelerators," Ph.D. Dissertation, Dept. of Mechanical and Aerospace Engineering, Thesis No. 3102-T, Princeton Univ., Princeton, NJ, June 2002.

[19]Markusic, T. E., Choueiri, E. Y., and Berkery, J. K., "Measurements of Current Sheet Canting in a Pulsed Electromagnetic Accelerator," *Physics of Plasmas*, Vol. 11, No. 10, 2004, pp. 4847–4858.